Mg $3pnd$ ($J=3$) autoionization spectra using isolated-core excitation

C. J. Dai, G. W. Schinn, and T. F. Gallagher
Department of Physics, University of Virginia, Charlottesville, Virginia 22901
(Received 29 January 1990)

The Mg $3pnd$ $J=3$ autoionizing spectra have been studied for n values ranging from 9 to 40, using an isolated-core excitation technique with ion detection. The measured spectra are found to be in generally excellent agreement with results from a calculated reaction matrix. The observed spectra exhibit strong interseries interactions between the $3p_{1/2}nd_{5/2}$ and $3p_{3/2}nd_j$ series, and, for $n \leq 15$, interferences between the amplitudes for excitation of the core electron to the $3P_{1/2}$ and $3P_{3/2}$ ion states. Classifications of states for $n \leq 29$ are tabulated. We discuss the difficulties in deducing autoionization rates for Mg from the experimental and theoretical data, the implications of which could have relevance to dielectronic recombination rate calculations.

INTRODUCTION

In recent years a number of experimental and theoretical[1,2] studies have been undertaken of autoionization of doubly excited alkaline-earth atomic states. The isolated-core excitation technique[3] (ICE) has enabled production of a large number of well-defined autoionizing states, many of which cannot be reached from the ground state by photoionization on account of selection-rule restrictions. Furthermore, with this method there is virtually no continuum excitation, and hence the resulting spectra are not complicated by interferences between discrete and continuum excitations.

We report here the study of the $3pnd(J=3)$ doubly excited states in magnesium using ICE for n ranging from 9 to 40. These experimental data are in very good accord with calculated spectra. Earlier experimental investigations of ICE in alkaline-earth elements have focused on barium,[4-6] strontium,[3,7] and calcium.[8] Apart from some preliminary results by Bonanno *et al.*,[9] magnesium has not been previously studied using this technique. Magnesium differs from the previously investigated alkaline-earth atoms in that its lowest-lying ms and mp ion states ($m=3$ for Mg) are not accompanied by a lower-lying $(m-1)d$ state. Thus, there are only two continua into which the Mg doubly excited states may decay (below the Mg^+ $3P_{1/2}$ limit), compared with 12 for the analogous system in the heavier alkaline-elements. The existence of only two continua makes interference effects more prominent and allows a more complete modeling of the autoionization process. Additionally, the fine-structure splitting of the Mg^+ $3P_{1/2}$ and $3P_{3/2}$ terms (92 cm^{-1}) is much less than the splitting of the equivalent terms in the heavier alkaline-earth elements (cf. 220 cm^{-1} in Ca^+, ~ 800 cm^{-1} in Sr^+, and ~ 2000 cm^{-1} in Ba^+). The smaller splitting has two manifestations. First, members of the series converging to the Mg^+ $P_{1/2}$ limit can interact with members of the $3p_{3/2}nd_j$ series having n values as high as 35. Second, for $n \sim 13$, the Δn interval between the Rydberg states of either series is equal to the difference in the series limits. As a result, there are often comparable excitation amplitudes to series converging to the $3P_{1/2}$ and $3P_{3/2}$ limits, leading to spectra with notable interference effects, which are effectively absent in the ICE spectra of the heavier elements.

Over the past decade, two approaches have been taken to match experimental data to the multichannel quantum-defect theory (MQDT), the theoretical method that provides the best physical description of the underlying atomic dynamics.

The first approach is still frequently used and involves the empirical determination of a set of parameters representing the interaction between specific channels by fitting the measured peak positions and widths of the autoionizing states. However, this can prove rather cumbersome, especially when many channels are involved. Furthermore, if the observed spectra exhibit narrow peaks, the widths of which are limited by the laser linewidth or other experimental effects, such fitting may not be feasible.

The second, more recent, approach utilizes an eigenchannel $\underline{R}$-matrix method calculation combined with MQDT for the atomic species of interest.[10] For a particular total angular momentum J, the resulting nearly energy-independent reaction matrix $\underline{K}$ may then be used to calculate the autoionizing spectra arising from excitation from any initial state. Most of the computational difficulty is associated with calculation of the $\underline{K}$ matrix; once evaluated, it is straightforward to synthesize spectra corresponding to excitation from a different initial state. Thus this is the approach used here. Greene[11] has calculated the $\underline{K}$ matrix relevant to this $J=3$ odd-parity problem, and we use his $\underline{K}$ matrix to calculate synthetic spectra. These spectra are compared to the experimental results, as described below.

EXPERIMENTAL APPROACH

Population of the Mg $3pnd$ states is effected by multistep laser excitation of the atoms in an effusive beam to autoionizing doubly excited states, followed by detection of the ions resulting from the decay of the autoionizing atoms. Figure 1 illustrates the three excitation steps used, along with their associated laser wavelengths. An

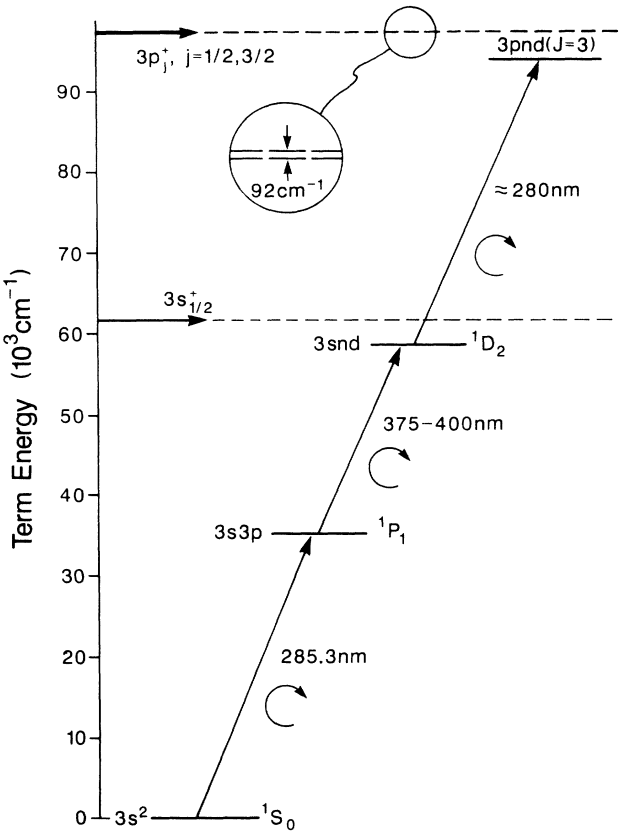

FIG. 1. ICE excitation scheme used in this experiment. One valence electron is prepared in a $3snd(n=9-40)$ Rydberg state, and the second electron is excited by the third step.

advantage of this stepwise excitation method is that only relatively low laser powers are required, as the laser-driven ion transitions are single-electron transitions, two of which are the resonance lines of the neutral and ion species, respectively. All three steps require the exciting photons to be circularly polarized in the same sense, in order that the final $3pnd$ states have $J=3$. The rather short wavelengths required in this scheme necessitate the use of frequency doubling or mixing crystals for each step. This complication is probably the principal reason for the heavier alkaline-earth elements having been studies first; their excitation wavelengths lie in regions that can be directly produced by dye lasers.

Figure 2 schematically illustrates the experimental apparatus. An approximately 5-ns-long, second-harmonic pulse from a Quanta-Ray DCR-1 Nd:YAG laser (not shown) is used to pump all three dye lasers. Dye lasers 1 and 3 are of the Littman design,[12] and dye laser 2 is a commercial model (Quanta-Ray PDL) that uses the Hänsch design.[13] The linewidth of all three lasers is $\simeq 0.8$ cm^{-1}.

The output from the first laser is passed through a potassium dihydrogen phosphate (KDP) doubling crystal to yield the 285.3-nm wavelength necessary for excitation of the $3s-3p\ ^1P_1$ resonance level. The term energy of this level (35 051.3 cm^{-1}) is greater than half the ionization energy (61 671.02 cm^{-1}), and hence two-photon or two-step excitation of the ground-state atoms into the continuum can occur with the first laser alone. Thus it is important that the frequency-doubled radiation be sufficiently attenuated in order that the ion signal cannot be observed when only the first laser beam excites the atoms.

The output from the second laser is mixed with some

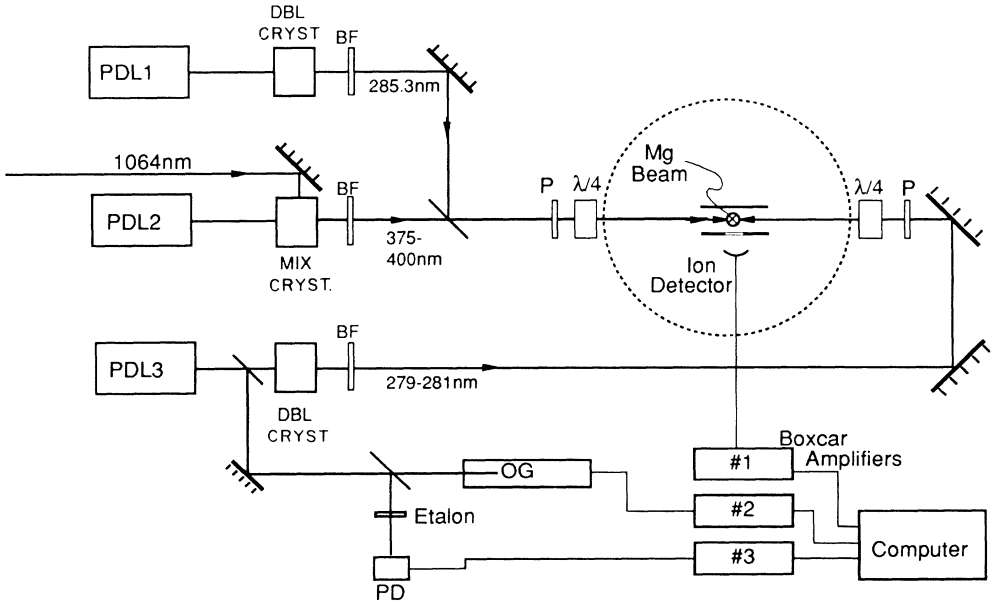

FIG. 2. Schematic of experimental setup, as described in text. PDL: Nd:YAG-pumped pulsed dye laser; BF: blocking filter passing only short-wavelength beam generated in crystal; OG: argon optogalvanic tube used to provide absolute frequency scale; PD: photodiode detecting etalon fringes to linearize scan; DBL CRYST.: KDP doubling crystal; MIX CRYST.: KDP mixing crystal.

of the residual 1064-nm Nd:YAG fundamental beam in a KDP crystal, to produce tunable radiation in the 400–375-nm range necessary to excite $n=9$–40. During a scan, this laser is fixed at a wavelength appropriate to the desired n value.

The output from the third laser is also frequency doubled with a KDP crystal. For most scans, the laser is tuned so that this doubled radiation covers a $\lesssim 200$ cm^{-1} range about the $\simeq 280$-nm wavelength necessary to excite the Mg^+ $3s-3p$ transitions. A servomechanical device (Inrad Autotracker II) is used to maintain the phase-matching condition for frequency doubling by continuously adjusting the crystal angle as the frequency of the third laser is scanned.

In order for the frequency of the third laser to be put on an absolute scale, the part of the laser fundamental frequency remaining after the beam passes through the doubling crystal is sent into an argon discharge tube, and the optogalvanic signal monitored as the laser is scanned. Another part of this $\simeq 560$-nm fundamental is passed through an étalon (free spectral range equal to 3.264 cm^{-1}), and the resultant fringes monitored on a photodiode. Using a least-squares regression method, the fringe spacings are fit to a third-order polynomial, which then is used to correct nonlinearities in the scan.

The beams from the first and second lasers are made coincident, and circularly polarized using a Glan prism and rhomb combination. They then pass into the vacuum chamber through a fused-silica window. The third laser is independently polarized with another Glan prism and rhomb before entering the chamber from the opposite direction.

The effusive Mg atomic beam, produced by resistive heating of an oven, passes between two 8×8-cm^2 field plates separated by 1 cm. The laser beams interact with the atomic beam in the central region between the two plates. An approximately +9-V pulse, applied to the bottom plate $\simeq 1\mu$s after the laser pulse, pushes ions arising from the autoionizing atoms through a mesh on the grounded upper plate, where they are detected by a particle multiplier. Typical background pressure during scans is 3×10^{-6} Torr.

The lasers are fired at a repetition rate of 12 Hz. The resultant ion signals are amplified, sent through a gated integrator, and stored in a microcomputer, while the third laser is scanned slowly (typically 10–20 cm^{-1}/min). Also stored in the same data file are the corresponding optogalvanic and étalon-fringe signals.

Tests were performed to confirm that the integration time on the ion-signal gated integrator is small enough not to introduce a measurable width to sharp spectral features beyond that already attributable to the nonzero laser linewidth.

SYNTHESIS OF SPECTRA FROM THE $\underline{K}$ MATRIX

As mentioned above, we have calculated spectra using a reaction matrix calculated by Greene,[11] in conjunction with parameters appropriate to our excitation scheme. There are eight possible odd-parity $J=3$ channels below the Mg^+ $3p$ states, as listed in Table I. In the calculations we have included only the five configurations corresponding to $3p\epsilon d$ and $3s\epsilon f$ and have ignored the $3p\epsilon g$ configurations. Our neglect of all states converging to higher Mg^+ states seems well justified, since the lowest one, the $3d^+$ limit, lies $\sim 35\,000$ cm^{-1} above the $3p^+$ limit. As a result, the effective quantum number of a doubly excited $3dnl$ state is very low, $\simeq 3.5$, in the region of the $3pn'd$ ($n'=9$–40) states. Since the lifetime of Rydberg series members scales as ν^3, where ν is the effective quantum number (equal to $n-\delta$, δ being the quantum defect of the series), such a $3dnl$ state should be very short lived. Any contribution from it to the observed spectra should be very broad, yielding a small overall increase in the background. On the other hand, the $3p\epsilon g$ configuration might be expected to have a greater influence than $3d\epsilon p$ on the spectra. These high-l states should have quantum defects of approximately zero. Of the 11 experimental spectra from $n=10$–20, only four exhibit features at or near energies associated with zero quantum defect, and hence one cannot neglect $3png$ states *a priori*. However, the finally synthesized spectra match the experimental scans very well without these configurations, providing an *a posteriori* justification for their exclusion. The observation of features at or near zero quantum defect (reproduced in the calculations) seems coincidental. The five channels used in this analysis and their mutual interactions are shown schematically in Fig. 3.

TABLE I. The eight jj-coupled and LS-coupled series with $J=3$ and odd parity, each having a limit at or below the Mg^+ $3P_{3/2}$ ion limit.

$3s_{1/2}\epsilon f_{5/2}$	$3p\epsilon d\,^3D^o_3$
$3s_{1/2}\epsilon f_{7/2}$	$3s\epsilon f\,^1F^o_3$
$3p_{1/2}\epsilon d_{5/2}$	$3p\epsilon d\,^1F^o_3$
$3p_{3/2}\epsilon d_{3/2}$	$3s\epsilon f\,^3F^o_3$
$3p_{3/2}\epsilon d_{5/2}$	$3p\epsilon d\,^3F^o_3$
$3p_{1/2}\epsilon g_{7/2}$	$3p\epsilon g\,^1F^o_3$
$3p_{3/2}\epsilon g_{7/2}$	$3p\epsilon g\,^3F^o_3$
$3p_{3/2}\epsilon g_{9/2}$	$3p\epsilon g\,^3G^o_3$

Greene has evaluated the reaction matrices at three energies, for the three LS-coupled terms by which the $J=3$, odd-parity, $3p\epsilon d$ and $3s\epsilon f$ configurations may be described. These energies, at -0.40, -0.39, and -0.38 a.u. below the lowest-lying Mg^{2+} limit, correspond to Mg term energies of 95 148.8, 97 343.5, and 99 538.3 cm^{-1}. In our calculations the energy-interpolated $\underline{K}^{LS}$ matrix is found by fitting a parabola to the values at these three energies. The blocks comprising these matrices are presented in Table II. (It should be emphasized that use of these matrices is not restricted to $J=3$ states. For instance, the same ^3D $\underline{K}$ matrix, given here as a 1×1 subblock, is also among the matrices included in the evaluation of the $J=1$ spectra.) The procedure used to synthesize the

spectra from these matrices will now be outlined, expanding upon the description given by Greene and Kim[14] and Lee and Lu.[15]

The $\underline{K}^{LS}$ need to be transformed from LS-coupling to the jj-coupled *dissociation channels* most suitable for MQDT analysis. This orthogonal 5×5 transformation matrix $\underline{V}$ is evaluated using standard $3n-j$ tables[16] and presented along with the LS- and jj-coupled states:

$$\begin{bmatrix} 3s_{1/2}\epsilon f_{5/2} \\ 3s_{1/2}\epsilon f_{7/2} \\ 3p_{1/2}\epsilon d_{5/2} \\ 3p_{3/2}\epsilon d_{3/2} \\ 3p_{3/2}\epsilon d_{5/2} \end{bmatrix} = \begin{bmatrix} 0 & \sqrt{3/7} & 0 & \sqrt{4/7} & 0 \\ 0 & \sqrt{4/7} & 0 & -\sqrt{3/7} & 0 \\ \sqrt{2/9} & 0 & -\sqrt{1/3} & 0 & \sqrt{4/9} \\ -\sqrt{1/15} & 0 & \sqrt{2/5} & 0 & \sqrt{8/15} \\ \sqrt{32/45} & 0 & \sqrt{4/15} & 0 & -\sqrt{1/45} \end{bmatrix} \begin{bmatrix} 3p\epsilon d\ ^3D \\ 3s\epsilon f\ ^1F \\ 3p\epsilon d\ ^1F \\ 3s\epsilon f\ ^3F \\ 3p\epsilon d\ ^3F \end{bmatrix} . \tag{1}$$

This $\underline{V}$ may then be used to transform $\underline{K}^{LS}$ into the jj-coupled basis using

$$\underline{K}^{jj}=\underline{V}^T\underline{K}^{LS}\underline{V} . \tag{2}$$

$\underline{K}^{jj}$ may be in turn diagonalized:

$$(\underline{K}^{jj})_{ij}=\sum_\alpha U_{i\alpha}\tan(\pi\mu_\alpha)(U_{\alpha j})^T , \tag{3}$$

where $\underline{U}$ is the 5×5 unitary transformation and $\tan(\pi\mu_\alpha)$ are the eigenvalues of K_{jj}. Alternatively, one can find the 5×5 eigenvector matrix that diagonalizes $\underline{K}^{LS}$ and then multiply it by the $jj-LS$ transformation to yield $U_{i\alpha}$.

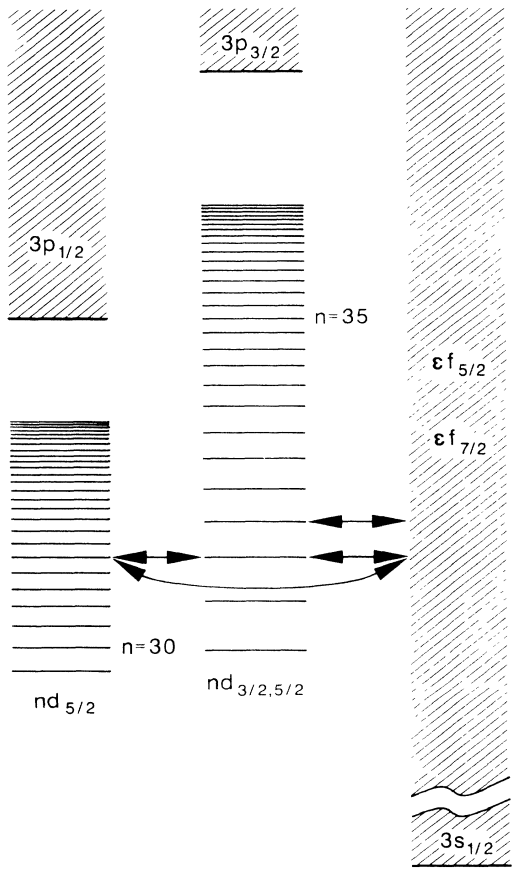

FIG. 3. Illustration of interseries interaction and continuum decay channels for the autoionizing Rydberg series studied here.

For brevity, we number the five jj-coupled dissociation channels in Eq. (1) from 1 to 5, beginning with $3s_{1/2}f_{5/2}$. Channels 1 and 2 are *open* —that is, their limit lies below the $\sim96\,000$-cm^{-1} term energy of the final, laser-excited state. Channels 3, 4, and 5 are *closed,* channel 3 having an effective quantum number ν_3 with respect to the Mg^+ $3P_{1/2}$ limit and channels 4 and 5 having an effective quantum number $\nu_4(=\nu_5)$ with respect to the $3P_{3/2}$ limit.

The wave function describing the electron and ion system following autoionization is termed a *collision eigenstate.* There are as many of these collision eigenstates as there are open channels, and each collision eigenstate $\Psi^{(\rho)}$ corresponds to a linear combination of the open channels with the same highly energy-dependent continuum phase $-\pi\tau_\rho$.

Each $\Psi^{(\rho)}$ may be expressed as a linear combination of close-coupling eigenchannels $\psi_{\rho\alpha}$:

$$\Psi^{(\rho)}=\sum_\alpha B_\alpha^{(\rho)}\psi_{\rho\alpha} \tag{4a}$$

or of the dissociation channels $\phi_{\rho i}$,

$$\Psi^{(\rho)}=\sum_i A_i^{(\rho)}\phi_{\rho i} . \tag{4b}$$

Each close-coupled wave function includes a scattering phase $-\pi\mu_\alpha$, and each dissociation channel includes a phase shift of $\pi\nu_i$ for the closed channels and $-\pi\tau_\rho$ for the open channels.

The close-coupled eigenchannels naturally satisfy the $r=0$ boundary condition, and the dissociation channels naturally satisfy the $r=\infty$ boundary condition. The dissociation-channel wave functions are related to the close-coupled-channel wave functions by the unitary transformation $U_{i\alpha}$ defined by Eq. (3). We take advantage of this fact to express the wave function in a form that simultaneously satisfies the $r=0$ and $r=\infty$ boundary conditions. This procedure leads to[15,17]

$$A_i^{(\rho)}=\sum_\alpha U_{i\alpha}\cos[\pi(\nu_i+\mu_\alpha)]B_\alpha^{(\rho)} , \tag{5a}$$

$$0=\sum_\alpha U_{i\alpha}\sin[\pi(\nu_i+\mu_\alpha)]B_\alpha^{(\rho)} . \tag{5b}$$

A nonzero solution exists to $B_\alpha^{(\rho)}$ if

TABLE II. Elements of the matrix blocks comprising the 5×5 block-diagonal $\underline{K}$ matrices calculated by Greene (Ref. 11) corresponding to the three energies (in atomic units with respect to the Mg^{2+} ground-state limit) used in this analysis.

	$^3D^\circ$	$^1F^\circ$		$^3F^\circ$	
Energy (a.u.)	$3p\epsilon d$	$3s\epsilon f$	$3p\epsilon d$	$3s\epsilon f$	$3p\epsilon d$
-0.40	0.582 377 58	0.234 298 34	0.674 580 65	0.240 425 48	0.814 795 71
		0.674 580 65	-0.311 813 84	0.814 795 71	2.035 945 04
-0.39	0.605 326 03	0.210 405 33	0.697 276 64	0.208 646 82	0.735 945 24
		0.697 276 64	-0.283 218 73	0.735 945 24	1.880 731 93
-0.38	0.632 968 65	0.184 781 09	0.715 751 12	0.183 114 13	0.670 628 29
		0.715 751 12	-0.257 400 59	0.670 628 29	1.756 003 40

$$\det\{U_{i\alpha}\sin[\pi(\nu_i+\mu_\alpha)]\}=0\ . \tag{6}$$

In Eqs. (5) and (6), ν_i is replaced by $-\tau_\rho$ for the open channels ($i=1,2$ in this case, for term energies below the $3P_{1/2}$ limit of Mg^+, and $i=1,2,3$ for energies between the two $3P$ limits). Equation (6) determines the possible values of τ_ρ.

We first consider energies below the $3P_{1/2}$ limit. In this energy range there are two open channels, and numerical evaluation of Eq. (6) yields two distinct τ_ρ values at each energy.

The labeling of each of these two resulting τ curves with a particular ρ value is unimportant for the calculation of the ICE spectra. Our ion-detection method cannot distinguish between the two open channels, and hence the observed cross section involves the sum of the squares of the two ρ-dependent partial cross sections, as will be shown below.

For each τ_ρ at each energy, Eq. (5b) can be used to obtain the five $B_\alpha^{(\rho)}$. Equation (5a) can be used in turn to obtain the corresponding $A_i^{(\rho)}$.

The amplitude for excitation of collision eigenstate $\Psi^{(\rho)}$ from the initial Rydberg state $|a\rangle$ is given by a summation over the closed dissociation channels, viz.,

$$D_\rho=\langle\Psi^{(\rho)}|\mathbf{r}|a\rangle=\sum_{i=3,4,5}\langle i|\mathbf{r}|a\rangle A_i^{(\rho)}\ , \tag{7}$$

where the $A_i^{(\rho)}$ are scaled to produce a wave function normalized per unit energy.[15] The normalization integral only depends upon the open channels $i=1,2$:

$$N_\rho=\sum_{i=1,2}\left|\sum_\alpha U_{i\alpha}\cos[\pi(-\tau_\rho+\mu_\alpha)]B_\alpha^{(\rho)}\right|^2\ . \tag{8}$$

Since we are unable to excite the Mg $3snd\ ^3D_2$ states we infer that the initial $3snd\ ^1D_2$ Rydberg state $|a\rangle$ should be well described by LS coupling. It may be re-expressed in jj-coupling as $\alpha_{3/2}|3s_{1/2}nd_{3/2}\rangle+\alpha_{5/2}|3s_{1/2}\ nd_{5/2}\rangle$, where $\alpha_{3/2}=(\frac{2}{5})^{1/2}$ and $\alpha_{5/2}=(\frac{3}{5})^{1/2}$.

TABLE III. $J=3$ matrix elements for the angular part of the dipole transition amplitude.

$\langle 3p_{1/2}vd_{5/2}\|\mathbf{r}_\Omega\|3s_{1/2}nd_{5/2}\rangle=$const
$\langle 3p_{3/2}vd_{3/2}\|\mathbf{r}_\Omega\|3s_{1/2}nd_{3/2}\rangle=-1.341\,64\times$const
$\langle 3p_{3/2}vd_{5/2}\|\mathbf{r}_\Omega\|3s_{1/2}nd_{5/2}\rangle=-0.894\,43\times$const

The dipole matrix element may be written as a product of radial and angular factors. Thus

$$\langle i|\mathbf{r}|a\rangle=\langle i(r)|\mathbf{r}_r|a(r)\rangle\langle i(\Omega)|\mathbf{r}_\Omega|a(\Omega)\rangle$$
$$=\sum_{j=\frac{3}{2},\frac{5}{2}}\alpha_j\langle 3p_{J_i}|\mathbf{r}_r|3s_{1/2}\rangle\langle\nu'_{J_i}l_k|\nu d_j\rangle$$
$$\times\langle 3p_{J_i}\nu'_{J_i}l_k|\mathbf{r}_\Omega|3s_{1/2}nd_j\rangle\delta_{jk}\delta_{2l}\ , \tag{9}$$

where $J_i=\frac{1}{2}$ for $i=3$, and $J_i=\frac{3}{2}$ for $i=4,5$. $\langle\nu'_{J_i}l|\nu l\rangle$ is the overlap integral between the outer wave function in the bound nl state of effective quantum number ν [binding energy $-(1/2\nu^2)$] and the autoionizing $\nu'l$ channel at the energy given by effective quantum number ν'_{J_i} relative to the $3p_{J_i}$ ion limit. It may be expressed as[18]

$$\langle\nu'|\nu\rangle=\langle\nu'l|\nu l\rangle=\frac{2(\nu\nu')^2}{\nu^{3/2}\pi(\nu'^2-\nu^2)}\sin\pi(\nu'-\nu)\ . \tag{10}$$

It is useful to note that $\langle\nu'|\nu\rangle$ has a width of $1/\nu^3$. If this width is much less than the Mg^+ fine-structure interval, amplitudes to the $3p_{1/2}nd_{5/2}$ series and $3p_{3/2}nd_j$ series do not overlap and therefore do not interfere. On the other hand, if the width of $\langle\nu'|\nu\rangle$ is greater than or equal to the Mg^+ $3p$ fine-structure interval, interference in the excitation amplitudes is significant. We shall return to consider this point explicitly.

The $\langle 3p_{J_i}\nu_{J_i}d_j|\mathbf{r}_\Omega|3s_{1/2}nd_j\rangle$ are calculated using angular momentum algebra[16] and are listed in Table III. Also, note that

$$\langle 3p_{1/2}|\mathbf{r}_r|3s_{1/2}\rangle\simeq\langle 3p_{3/2}|\mathbf{r}_r|3s_{1/2}\rangle\ ,$$

since the Coulombic force varies little for these two cases.

The energy-dependent amplitude for excitation of collision eigenchannel ρ is found by combining Eqs. (7) and (9), yielding

$$D_\rho=\pm\text{const}'[-\langle\nu'_{1/2}|\nu\rangle A_3^{(\rho)}+\langle\nu'_{3/2}|\nu\rangle(1.095\,45\,A_4^{(\rho)}+0.894\,43\,A_5^{(\rho)})]\ , \tag{11}$$

where the upper and lower signs correspond to all the laser beams inducing $\Delta m=\pm1$ transitions, respectively.

The observed cross section for excitation of these doubly excited $J=3$ states is given by

$$\sigma = \text{const} \times \omega \sum_{\rho=1,2} |D_\rho|^2 , \tag{12}$$

where ω is the third-laser frequency. Clearly the polarization helicity of the three laser beams is unimportant, provided that all three are polarized with the same sense.

Above the $3P_{1/2}$ limit, there are three open channels ($3s\epsilon f_{5/2,7/2}$, $3p_{1/2}\epsilon d_{5/2}$) and two closed channels ($3p_{3/2}nd_{3/2,5/2}$). These three open channels result in three eigenphase shifts τ_ρ at each energy. The $3p_{3/2}nd_j$ states lying above the $3P_{1/2}$ limit have $n > 35$. The width of an overlap integral from a bound $3snd$ state is $\sim 1/n^3$, and hence for $n > 35$ this width is $< 5\text{cm}^{-1}$, a width far smaller than the Mg^+ $3p$ fine-structure splitting of 92 cm^{-1}. In this case the overlap integrals for the excitation to the $3p_{1/2}nd_{5/2}$ channel and to the $3p_{3/2}nd_j$ channels do not overlap significantly, and we may ignore the excitation amplitude to the $3p_{1/2}\epsilon d_{5/2}$ channel when calculating the spectra of the $3p_{3/2}nd_j$ states. In this approximation the amplitudes for each excitation channel are determined as in Eq. (11), and their sum yields the cross section, as in Eq. (12). Thus

$$\sigma = \text{const}\omega \langle \nu'_{3/2}|\nu\rangle^2 \sum_{\rho=1}^{3} (1.095\,45 A_4^{(\rho)} + 0.894\,43 A_5^{(\rho)})^2$$

$$= \text{const} \times \omega \langle \nu'_{3/2}|\nu\rangle^2 Z^2 , \tag{13}$$

where Z^2 is an effective spectral density. Hence, the synthesized spectra given by Eq. (13) can be regarded as the square of the overlap integral for the $p_{3/2}$ series times the effective spectral density.

RESULTS

Spectra of the Mg $3pnd(J=3)$ states were measured for all n values between 9 and 40 inclusive. Nonlinearities in these wavelength scans have been corrected, and they have put on an absolute frequency scale, as discussed earlier. At several n values, scans were repeated with the third-laser beam attenuated by a factor of 2 or 4, yielding essentially no change in the line shapes and relative amplitudes. This confirms that nonlinear effects (e.g., depletion broadening[19] or optical saturation) caused by the third-laser intensity are negligible.

Typical experimental spectra for $n=10$ and 23 are shown in Figs. 4 and 5. The locations of the Mg^+ $3S_{1/2}-P_{1/2}$ and $3S_{1/2}-P_{3/2}$ ion lines are also indicated. Also shown with each of these traces are the associated synthesized spectra. The overall agreement between the measured and calculated results is clearly very satisfactory.

Figure 6 shows scans for $n=15$, with and without circularly polarizing optics. The bottom trace represents excitation by linearly polarized light, and hence exhibits both $J=1$ and 3 features. Comparison of Figs. 6(a) and 6(b) enables one to identify the $J=1$ and $J=3$ peaks in the latter spectrum. The nearly total extinction of the generally sharper $J=1$ features when the laser beams are circularly polarized indicates that the degree of circular polarization is very good.

Experimental resolution of the narrow and closely spaced features seen in the computed spectra is limited by the instrumental linewidth. In order to account for this, Gaussian line shapes of varying widths were convoluted to the synthesized spectra, and a best overall fit to the measured data was found for a full width at half maximum (FWHM) of 1.3 cm^{-1}. This instrumental linewidth is most likely attributable to the linewidth of the frequency-doubled radiation, which is expected to be approximately $\sqrt{2}$ greater then the measured fundamental linewidth of $\simeq 0.8$ cm^{-1}. Figure 7 shows an $n=19$ scan, the corresponding calculated spectrum, and the same synthesized spectra convoluted with an effective instrumental resolution of 1.3 cm^{-1}. Figure 8 presents the same set of traces for $n=30$. The uppermost and lowermost traces are clearly in very good accord. However, a small but persistent discrepancy between theory and experiment is manifest in the rightward skewing of the $P_{3/2}$ bundle, as in Fig. 8. This effect is observed over a wide range of n values.

For n values ranging upwards from 19, the clutter in the spectra coalesces into two bundles associated with the Mg^+ $P_{1/2}$ and $P_{3/2}$ limits. For scans corresponding to the lowest measured n ($=9,10$), only a few features are seen in the spectra, although those features are generally

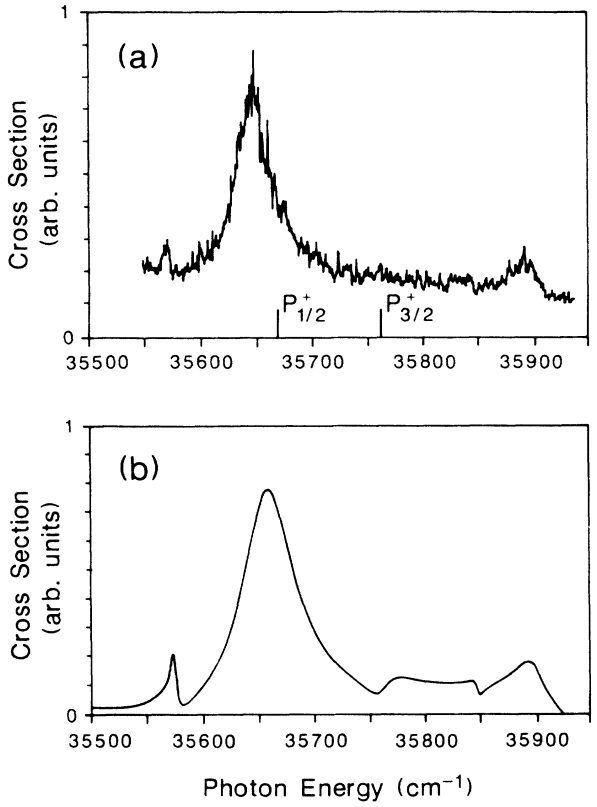

FIG. 4. (a) Detected ion signal as a function of third-step laser frequency for $3pnd, n=10$. (b) Spectrum synthesized from the $\underline{K}$ matrix for the same state. The small ($\sim 15\text{cm}^{-1}$ for $n=10$) shift of the theoretical curve occurs only for the lowest n studied; for $n \geq 11$, the agreement in peak locations is excellent. The energies of the Mg^+ $3s-3p$ resonance lines are indicated.

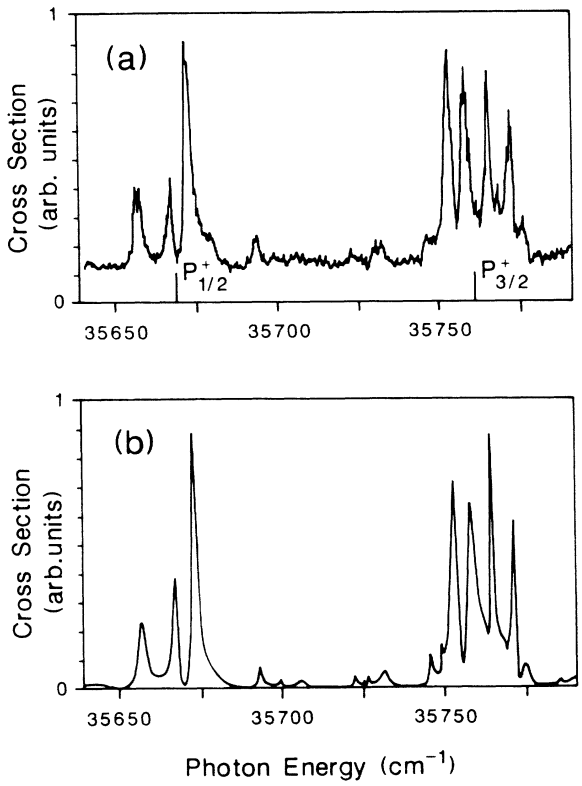

FIG. 5. Measured and calculated spectra for $3p23d$. The bundle of peaks with photon energy close to the $3S_{1/2}-3P_{3/2}$ ion transition have an interpeak spacing indicating that they originate from interseries interaction.

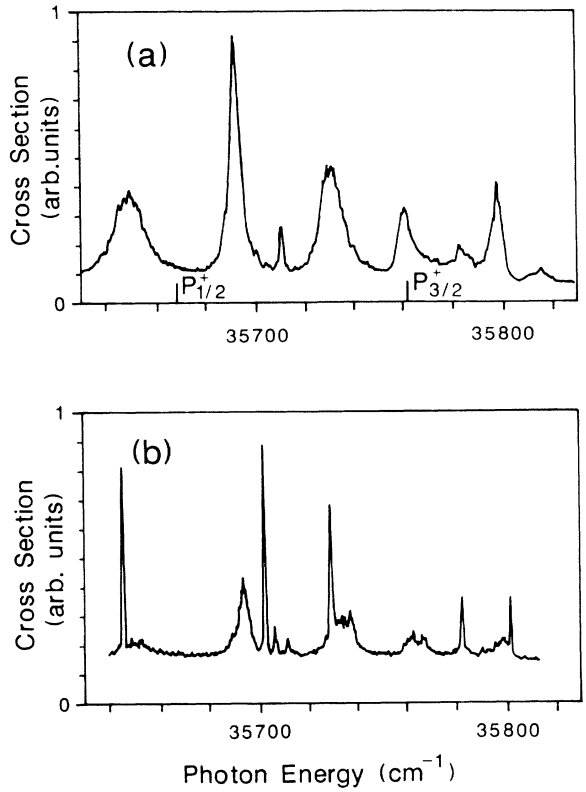

FIG. 6. Scan across $3p15d$ transitions with (a) all three lasers circularly polarized with the same sense, (b) all three lasers lineary polarized. The sensitivity of (b) is less than (a) by an uncalibrated factor. Note that several of the sharp features are almost completely extinguished with circular polarizaton, indicating that they are $J=1$.

wide and not clearly associated with a particular ion line. In fact, spectra calculated for these n over a much wider energy region show a great deal of structure, which is not seen in the experimentally limited scan range.

Interseries interaction is strong between the autoionizing states converging to the Mg^+ $3P_{1/2}$ and $3P_{3/2}$ limits. One interesting manifestation of these mutual interactions can be seen in the structure of the $P_{3/2}$ bundle and is most apparent in the higher-resolution calculated spectra. The superimposed sharp oscillations are due to perturbations from the nearly degenerate higher-n $p_{1/2}$ states (Fig. 3). For instance, Fig. 5 illustrates the superimposed $p_{1/2}$ $n\sim30$ peaks on the broad $3p_{3/2}23d_j$ resonance. In Fig. 8 the more closely spaced modulation of the $n=30$ $p_{3/2}$ bundle is due to the $n\sim60$ $p_{1/2}$ states. The spacing of these peaks matches the spacing expected between adjacent n for Rydberg series converging to the Mg^+ $P_{1/2}$ limit which have the same term energy as the lower-n $p_{3/2}$ features.

Members of the $3p_{3/2}nd_j$ series lie above the $P_{1/2}$ limit for n greater than 35. The $3p_{1/2}\epsilon d_{5/2}$ channel thus no longer adds structure to the $p_{3/2}$ spectral profile. However, the interchannel interaction remains, and the spectra are qualitatively indistinguishable from spectra such as Fig. 8 just below the $3P_{1/2}$ limit. This continuity is shown explicitly in Fig. 9(a), the observed spectrum of the $3p_{3/2}40d_j$ states in the vicinity of the $P_{3/2}$ ion resonance. The spectrum is nearly identical, apart from an energy scaling, to the corresponding features in Fig. 8. Also shown in Fig. 9 is the computed spectrum, found by multiplying the underlying spectral density shown in Fig. 9(d) with the overlap function of Fig. 9(c), as prescribed in Eq. (13).

Naively, one might have expected the spectral profiles to be very symmetric above the $P_{1/2}$ limit, as are the profiles of the analogous Ba $6p_{3/2}nd_j$ and Sr $5p_{3/2}nd_j$ states, but this is clearly not the case. Much of the asymmetry in the spectral density Z^2 shown in Fig. 9(d) may be attributed to interference in the A_4 and A_5 amplitudes. Moreover, the spectral density due to A_4 alone is very asymmetric; that corresponding to A_5 is more regular in appearance.

DISCUSSION

The strong interaction between the series converging to Mg^+ $3P_{1/2}$ and the two series converging to $3P_{3/2}$ can be shown by ignoring the interaction with the $3s\epsilon f_j$ continua and constructing a Lu-Fano plot[20] from our data for energies below the former limit (using data from $n=9$

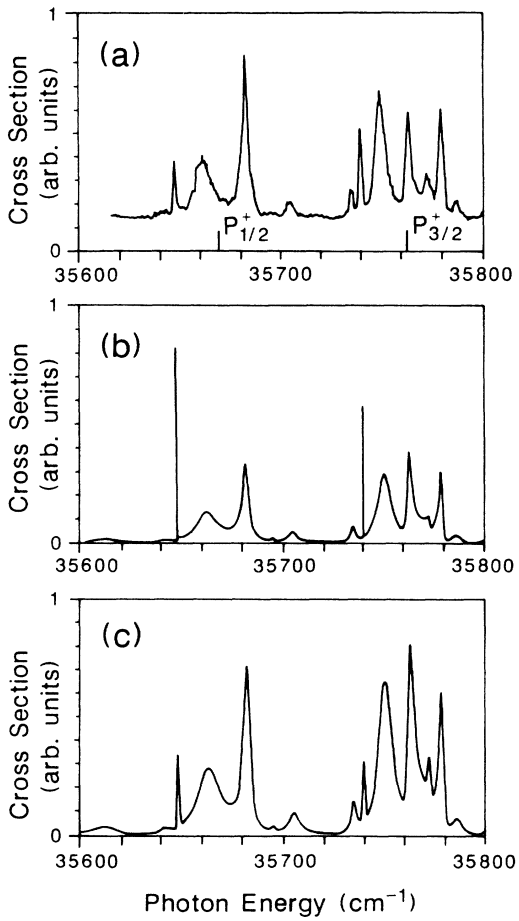

FIG. 7. $3p19d$ spectrum: (a) measured, (b) calculated from the $\underline{K}$ matrix, and (c) calculated including effective 1.3-cm^{-1} resolution.

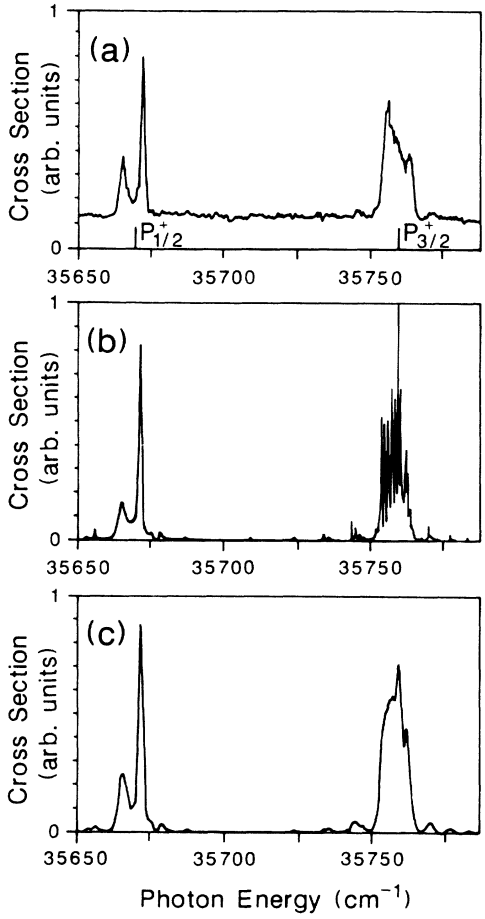

FIG. 8. $3p30d$ spectrum: (a) measured, (b) calculated, and (c) calculated with 1.3-cm^{-1} resolution.

to 26). Figure 10 shows two such plots, the upper one derived from the experimentally observed peak energies,and the lower plot constructed from the locations of the peaks in the synthesized spectra. The overall agreement between these two frames is a reflection of the generally excellent quality of the calculated spectra. In the absence of any interactions between the series, one would expect the Lu-Fano plot to consist of one horizontal and two vertical lines. The intercepts of these lines with the axes would correspond to the respective quantum defects of these (noninteracting) series. However, the behavior exhibited in Fig. 10 emphasizes that in actuality the interseries interaction is substantial.

The two-dimensional diagram of Fig. 10 is somewhat oversimplified and misleading, since interactions with the $3s\epsilon f$ continua have been neglected. An accurate graphical treatment requires the construction of a three-dimensional quantum-defect surface $\mathcal{S}$ defined by Eq. (6), as shown in Fig. 11. This surface consists of two sheets corresponding to the two values of τ_ρ, within a unit cube. The two sheets pass into each other upon translation by one unit in any of the $\nu_{1/2}$, $\nu_{3/2}$, or τ directions. Below the $P_{1/2}$ limit, $\nu_{1/2}$ and $\nu_{3/2}$ are related by the 92-cm^{-1} separation of the Mg^+ $3P_{1/2}$ and $3P_{3/2}$ limits. Explicitly,

$$\frac{1}{\nu_{3/2}^2}=8.35\times10^{-4}+\frac{1}{\nu_{1/2}^2}\ . \tag{14}$$

This equation is plotted for $\nu_{3/2}=19$ to 20 in Fig. 12, a range in which $\nu_{1/2}$ varies from 22.7 to 24.5. If plotted in the cube of Fig. 11, Eq. (14) would appear as sheets having an intersection with the $\nu_{1/2}$, $\nu_{3/2}$ plane given by Fig. 12. The locus defined by the intersection of these sheets with the surfaces in the three-dimensional surface $\mathcal{S}$ of Fig. 11 represents the path followed by the laser as it is scanned across the ion transitions. Autoionizing states occur where the phase τ is changing rapidly along this locus. This is simply a restatement of the fact that at each autoionizing resonance there is a phase shift of π. From the direction of the normal to $\mathcal{S}$, the character of the final-state wave function can be determined.

At any value of $\nu_{1/2}$ and $\nu_{3/2}$ along this locus, one can define the normals $\hat{\mathbf{n}}_\rho$ to the two sheets of $\mathcal{S}$ (each corresponding to one of the two τ_ρ). The components of $\hat{\mathbf{n}}_\rho$ in the $\nu_{1/2}$, $\nu_{3/2}$, and τ directions are proportional to the

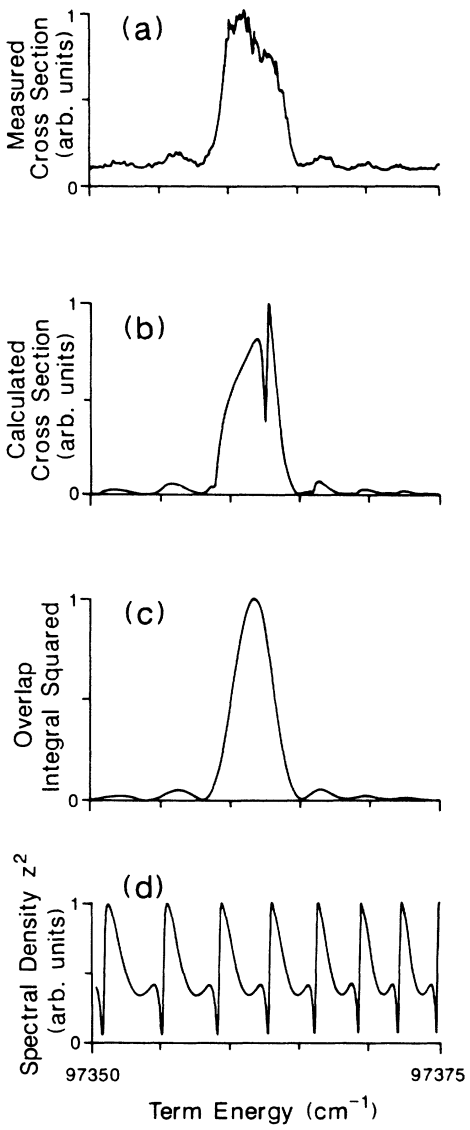

FIG. 9. Spectrum of $3p40d$ in region of the Mg^+ $P_{3/2}$ resonance: (a) measured, (b) calculated, (c) square of overlap integral associated with the $P_{3/2}$ state, and (d) effective spectral density Z^2 (as described in text).

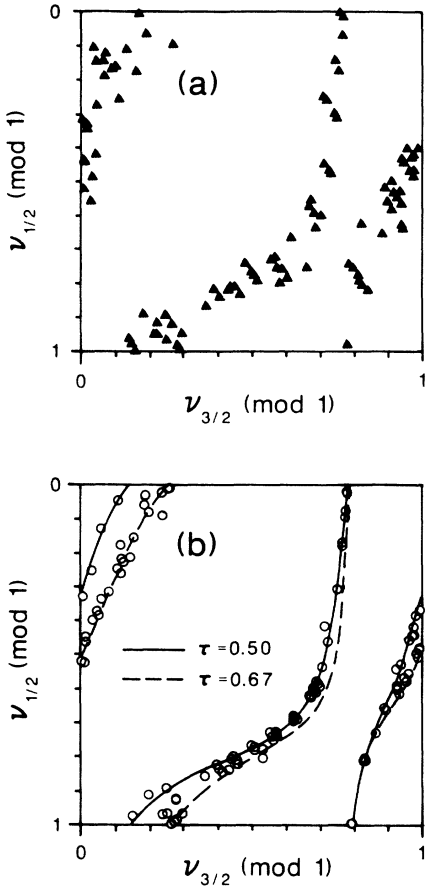

FIG. 10. Lu-Fano plots of peaks seen in final spectra: (a) determined from the measurements, (b) determined from the synthesized spectra. Each point represents a 3*pnd* feature in the range $n=9$–26. The points all fall within bands defined by τ values in the range 0.50 to 0.67.

spectral densities in the channels converging to the Mg^+ $3P_{1/2}$, $3P_{3/2}$, and $3S_{1/2}$ limits. As a result, inspection of the quantum-defect surface $\mathcal{S}$ allows one to associate the regions corresponding to mostly continuum, mostly $3p_{1/2}nd_{5/2}$ and mostly $3p_{3/2}nd_j$ with regions in which $\hat{\mathbf{n}}_\rho$ points along τ, $\nu_{1/2}$, and $\nu_{3/2}$, respectively.

With the underlying three-dimensional nature of the quantum-defect surface in mind, we return to the Lu-Fano plot of Fig. 10. This plot approximately matches the intersection of the surface $\mathcal{S}$ with a plane of constant τ_ρ for $0.50 < \mathrm{mod}_1(-\tau_\rho) < 0.67$. From the shape of this plot, one can deduce that the observed and calculated peaks correspond to $\mathrm{mod}_1(-\tau_\rho)$ values between 0.50 and 0.67, as indicated in Fig. 10b. In other words, it is only

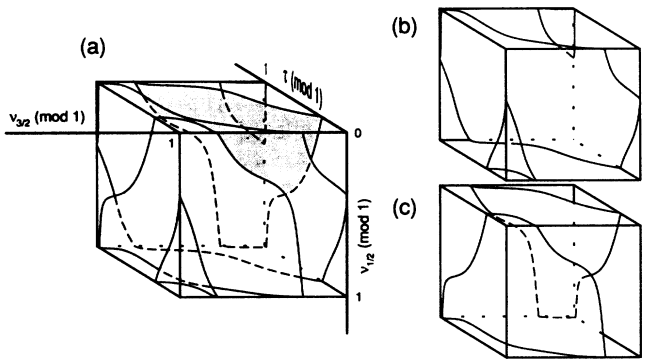

FIG. 11. (a) Three-dimensional quantum-defect surface plotted modulo 1 corresponding to the effective quantum number with respect to the Mg^+ $3P_{1/2}$ limit, the $3P_{3/2}$ limit, and the continuum phase above the $3S$ limit. For clarity, the two shaded surfaces are shown separately in (b), and the large central sheet and two small corner surfaces are shown in (c). The projection of the normal at any point on these surfaces along the three axes yields the composition of the state.

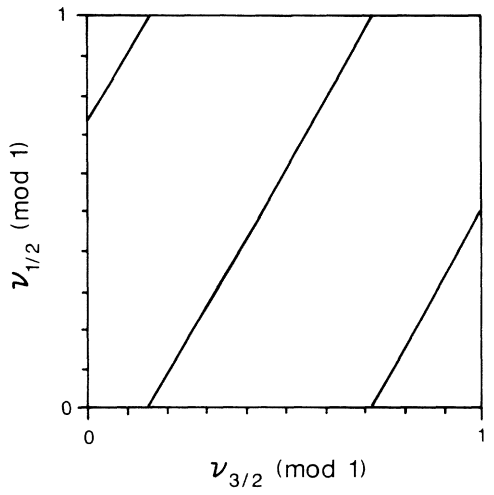

FIG. 12. The path taken by an excitation laser in the $\nu_{1/2}-\nu_{3/2}$ plane, as it is scanned in the range $3p_{3/2}\nu_{3/2}d, 19 \leq \nu_{3/2} \leq 20$. The intersection of this path with the surface of Fig. 14 defines the path followed in this three-dimensional quantum-defect space. Features in the spectral density occur where the continuum phase changes rapidly along this path.

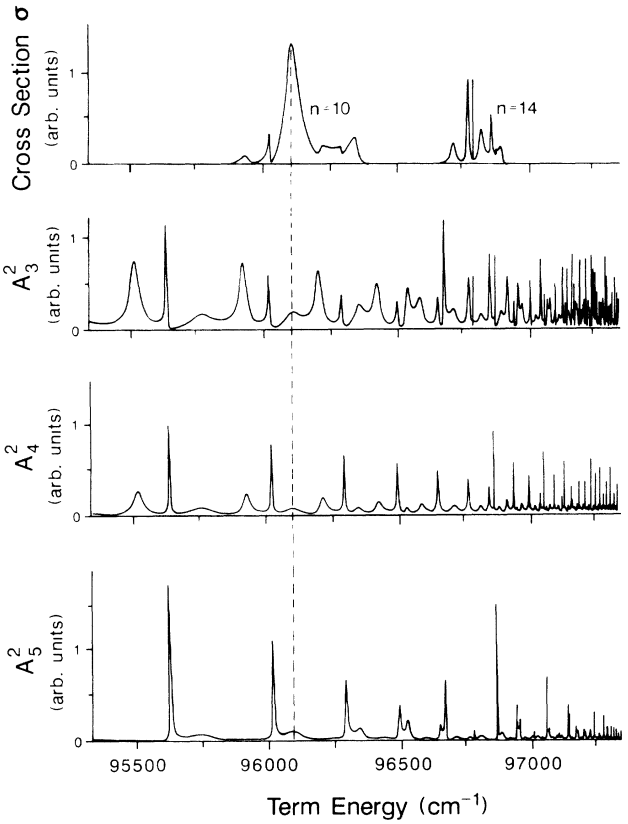

FIG. 13. All observed features in the final spectra correspond to features in the underlying spectral density. (The apparent strength depends upon the associated overlap integral as well.) For lower n values, the regularity apparent in the spectral densities corresponding to the three closed channels can be used to assign observed spectral features.

in this τ region that the locus defined by the intersection of Eq. (14) with $\mathcal{S}$ yields a wave function with a high degree of bound-channel character, and simultaneously satisfies the overlap-integral criterion of Eq. (10). Assuming that these peaks lie at the maximum phase shift from the underlying continuum phase, one expects the continuum phase to differ by 0.5, i.e., $\tau \sim 0.1$.

The complicated nature of the observed spectra makes a complete assignment of all the observed peaks not only a nearly impossible task, but also an effort of questionable utility. Nevertheless, in the range of $n=9$ to 29, we have classified most of the features by their term energies and have assigned them to either the $3p_{1/2}nd_{5/2}$, $3p_{3/2}nd_{3/2}$, or $3p_{3/2}nd_{5/2}$ series. This assignment was based upon the smoothly varying nature of the quantum defects corresponding to each of these three series. Additionally, the periodicity of the calculated spectral densities $A_i^2[=(A_i^{(1)})^2+(A_i^{(2)})^2]$, $i=3,4,5$ (Fig. 13) was used to aid in identification of each peak with a particular n. This periodicity is apparent in spite of the rather complicated structure for n values up to 14 (Fig. 13). For higher n, interseries interactions start to obscure the underlying pattern. Particular features in the observed spectra can be associated with features in the spectral densities, even though most of the structures are common to all three A_i^2. The periodicity of these features (which become progressively less clear for higher n values) provides an additional check on the quantum-defect-based assignments.

These classifications are presented in Table IV, for n values up to 29. We emphasize that the assignments of states to the specific jj-coupled series, although mutually consistent, are rather arbitrary, particularly in the case of the $3p_{1/2}nd_{5/2}$ states. From the Lu-Fano diagram of Fig. 10, it is evident that no feature can be accurately described as having almost exclusively $p_{1/2}$ character. (Such a state would have to lie along part of the quantum-defect curve having a normal nearly parallel to the $\nu_{1/2}$ axis.)

The rather small separation of the Mg^+ $3P_{1/2}$ and $3P_{3/2}$ limits gives rise to an important interference phenomenon between excitation amplitudes to the $3p_{1/2}nd_{5/2}$ and $3p_{3/2}nd_j$ channels. This effect is most pronounced at the lower n values (≤ 15), where the width of the overlap integral given by Eq. (10) is comparable to the spacing of the Mg^+ $3p$ states.

For n values less than or equal to 15, the central lobe of this overlap function is sufficiently broad that the $\langle \nu_j' | \nu \rangle$, $j=\frac{1}{2}, \frac{3}{2}$, each have significant amplitude 92 cm^{-1} from their respective centers, 92 cm^{-1} being the energy difference between the ion fine-structure states. In other words, an incident photon with an energy corresponding to the $P_{3/2}$ ion transition may excite the Rydberg atom in two possible ways. The first is, of course, excitation of the $P_{3/2}$ ion with the outer electron playing the role of a spectator. The second is excitation of the $P_{1/2}$ ion transi-

TABLE IV. Term energies and quantum defects of $3pnd, J=3$ states determined from experimental spectra. Estimated random uncertainty due to energy calibration and peak determination is $\pm 0.4\text{cm}^{-1}$ for most states.

State	Energy (cm^{-1})	Quantum defect	State	Energy (cm^{-1})	Quantum defect
$3p_{1/2}9d$	95 507.6	1.269	$3p_{3/2}9d_{3/2}$	95 616.9	1.224
			$9d_{5/2}$	95 737.0	0.954
$10d$	95 913.5	1.230	$10d_{3/2}$	96 005.1	1.230
			$10d_{5/2}$	96 082.5	0.982
$11d$	96 199.6	1.192	$11d_{3/2}$	96 279.6	1.242
			$11d_{5/2}$	96 329.7	1.022
$12d$	96 410.8	1.135	$12d_{3/2}$	96 481.0	1.258
			$12d_{5/2}$	96 514.3	1.064
$13d$	96 569.1	1.072	$13d_{3/2}$	96 634.1	1.272
			$13d_{5/2}$	96 654.6	1.119
$14d$	96 688.7	1.023	$14d_{3/2}$	96 749.9	1.315
			$14d_{5/2}$	96 789.6	0.929
$15d$	96 763.5	1.207	$15d_{5/2}$	96 853.5	1.226
			$15d_{5/2}$	96 873.7	0.979
$16d$	96 834.7	1.268	$16d_{3/2}$	96 938.8	1.082
			$16d_{5/2}$	96 961.1	0.732
$17d$	96 901.8	1.181	$17d_{3/2}$	96 985.1	1.329
			$17d_{5/2}$	97 006.9	0.932
$18d$	96 958.3	1.053	$18d_{3/2}$	97 049.7	1.057
			$18d_{5/2}$	97 063.0	0.752
$19d$	96 993.8	1.21	$19d_{3/2}$	97 086.1	1.19
			$19d_{5/2}$	97 095.8	0.93
$20d$	97 028.8	1.23	$20d_{3/2}$	97 124.7	1.10
			$20d_{5/2}$	97 132.5	0.86
$21d$	97 063.8	1.08	$21d_{3/2}$	97 156.9	1.02
			$21d_{5/2}$	97 164.3	0.75
$22d$	97 087.1	1.18	$22d_{3/2}$	97 174.9	1.34
			$22d_{5/2}$	97 183.4	0.99
$23d$	97 109.6	1.19	$23d_{3/2}$	97 198.1	1.33
			$23d_{5/2}$	97 204.5	1.03
$24d$	97 132.9	1.00	$24d_{3/2}$	97 222.5	1.11
			$24d_{5/2}$	97 226.9	0.86
$25d$	97 145.5	1.27	$25d_{3/2}$	97 242.1	0.95
			$25d_{5/2}$	97 245.9	0.71
$26d$	97 163.5	1.09	$26d_{3/2}$	97 253.9	1.17
			$26d_{5/2}$	97 256.1	1.01
$27d$	97 173.8	1.33	$27d_{3/2}$	97 269.6	1.00
			$27d_{5/2}$	96 271.8	0.82
$28d$	97 189.1	1.06	$28d_{3/2}$	97 280.1	1.12
			$28d_{5/2}$	97 283.8	0.78
$29d$	97 197.4	1.12	$29d_{3/2}$	97 291.4	1.05
			$29d_{5/2}$	97 294.6	0.73

tion instead, accompanied by an appropriate energy-conserving adjustment of the outer electron. The interference in the amplitudes for excitation through these two autoionization paths leads to the observed interference structure.

Of course, the above discussion is somewhat simplified. Interactions between the doubly excited Rydberg series corresponding to $P_{1/2}$ and $P_{3/2}$ limits markedly perturb the underlying spectral density, yielding new features and introducing significant additional shifts to the effective ion-line transition energies.

Interference effects in autoionization are ubiquitous. As examples, interferences between excitation of an autoionizing state embedded in the continuum and direct continuum excitation in ground-state photoionization leads to the well-known Beutler-Fano profile,[21] and interferences arising from Raman coupling to the singlet and triplet terms of an intermediate state can also be very pronounced.[22] In general, the effects observed are a function both of the excitation scheme used and the level structure of the species of interest. The ICE scheme is inherently insensitive to Beutler-Fano-type interferences,[1] and the near-rigorous LS coupling of the bound magnesium states results in very small amplitudes for excitation

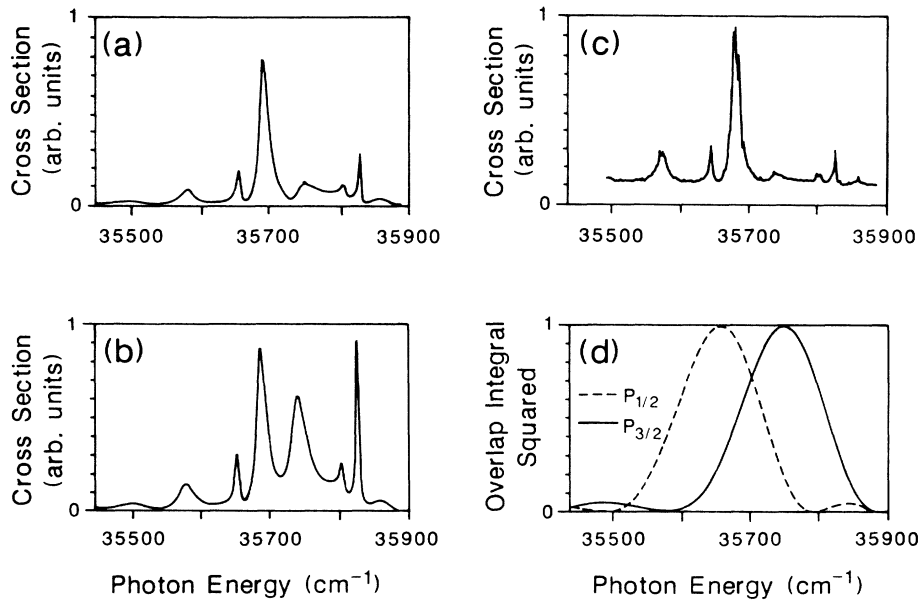

FIG. 14. Effect of "overlap interference": (a) Synthesized spectrum including interference, (b) same as (a) but using only direct-excitation terms, (c) measured spectrum, and (d) corresponding overlap integral squared.

of intermediate triplet states. The overlap interference observed here is a characteristic of the ICE technique. It is not observed as a major effect in previously studied elements because of the greater fine-structure splitting of their respective $ms-mp$ ion transitions. In these elements this competing excitation path has an amplitude proportional to the much-reduced higher-order lobes of the overlap function. Alternatively, one might view this interference effect as arising from the transition to LS coupling of the low-lying Mg $3pnd$ states.

The easiest way to show quantitatively the magnitude of this interference effect is to use Eq. (11) to write $|D_\rho|^2$ as a sum of *direct* and *interference* terms:

$$|D_\rho|^2=[(D_\rho)_{\rm dir}]^2+[(D_\rho)_{\rm int}]^2 , \tag{15}$$

where

$$[(D_\rho)_{\rm dir}]^2 \propto [A_3^{(\rho)}]^2\langle \nu'_{1/2}|\nu\rangle^2 + (1.095\,45\,A_4^{(\rho)}+0.894\,43\,A_5^{(\rho)})^2\langle \nu'_{3/2}|\nu\rangle^2 \tag{16a}$$

and

$$[(D_\rho)_{\rm int}]^2 \propto -2A_3^{(\rho)}(1.095\,45\,A_4^{(\rho)} + 0.894\,43\,A_5^{(\rho)})\langle \nu'_{1/2}|\nu\rangle\langle \nu'_{3/2}|\nu\rangle . \tag{16b}$$

Figure 14 illustrates the importance of this effect. Frame 14(a) presents the synthesized $3p12d$ autoionizing spectrum, frame 14(b) shows the spectra resulting from use of only the direct-excitation terms of Eq. (16a) in Eq. (12), frame 14(c) is the associated experimental spectrum, and the final frame shows the two overlap integrals corresponding to the Mg^+ $P_{1/2}$ and $P_{3/2}$ limits. For higher n values ($n>20$), overlap interference is much less important.

The complicated nature of the Mg $J=3$ spectra makes determination of the autoionization rates difficult. The interseries interactions and overlap-interference effects, in conjunction with the nonzero instrumental resolution, prevent useful information from being obtained by measurement of the peak widths, as can be done for simpler systems.[23] The calculated spectral densities are asymmetric, even above the limit (especially A_4^2). Hence the widths of their features cannot directly be interpreted in terms of rates. For this reason we do not present comprehensive quantitative results here.

CONCLUSIONS

The $3pnd$ $J=3$ spectra in magnesium appear considerably more complicated than their $mpnd$ counterparts in the previously studied alkaline-earth elements. The comparatively small, 92-cm^{-1} fine-structure splitting of the first-resonance ion states underlies much of this seeming irregularity. The heavier elements, with their larger splitting, also exhibit interseries interaction, but it occurs for correspondingly lower n values. Although the lack of a lower-lying $(m-1)d$ ion state in Mg aids in the theoretical modeling of the spectra, it is overshadowed by the complicating effects of interseries interaction. The small fine-structure spacing also is responsible for the importance of "overlap interference," an effect which is to ICE (under the appropriate conditions) as the Beutler-Fano profile is to ground-state photoionization.

Overlap interference is very prominent in Mg, for n

values ~ 13, mainly because the nl series of autoionizing states converging to the first excited p states of the ion are in intermediate coupling rather than jj-coupling, (that is, for this n the spacing between successive n levels approximates the fine-structure splitting). In the heavier alkaline-earth elements, this transition from jj coupling to intermediate coupling in autoionizing states converging to the ion first-resonance level occurs at lower n values and has been seen only in Ca.[24] Interestingly, the analogous states in beryllium, which has a 6.6-cm^{-1} Be^+ $2p$ fine-structure separation, should exhibit interference at $n \sim 30-35$. However, at lower n, the states become well described by LS coupling, and the interference effect should disappear.

The strong perturbations and interactions between the underlying spectral densities seen in this study indicate that the treatment of the doubly excited autoionizing states as "isolated resonances" in Mg dielectronic-recombination-rate calculations[25] may not be completely valid. The present study suggests that further consideration of the relationship between the spectral densities and the autoionizing rates is warranted.

Work is ongoing to extend this study to the Mg $3pns$ and $3pnd$ $J=1$ states and to analyze the angular distribution of the autoionizing electrons.

ACKNOWLEDGMENTS

We wish to thank R. R. Jones and W. Sandner for helpful discussions and are grateful to C. H. Greene for providing us with his K matrices. This work is supported by the U. S. Department of Energy, Division of Chemical Sciences, Office of Basic Energy Sciences.

[1]T. F. Gallagher, J. Opt. Soc. Am. B **4**, 794 (1987).
[2]W. Sandner, Comments At. Mol. Phys. **20**, 171 (1987).
[3]W. E. Cooke, T. F. Gallagher, S. A. Edelstein, and R. M. Hill, Phys. Rev. Lett. **40**, 178 (1978).
[4]F. Gounand, T. F. Gallagher, W. Sandner, K. A. Safinya, and R. Kachru, Phys. Rev. A **27**, 1925 (1983).
[5]R. Kachru, H. B. van Linden van den Heuvell, and T. F. Gallagher, Phys. Rev. A **31**, 700 (1985).
[6]J. Boulmer, P. Camus, and P. Pillet, J. Opt. Soc. Am. B **4**, 805 (1987).
[7]E. Y. Xu, Y. Zhu, O. C. Mullins, and T. F. Gallagher, Phys. Rev. A **33**, 2401 (1986).
[8]V. Lange, U. Eichmann, and W. Sandner, J. Phys. B **22**, L245 (1989).
[9]R. E. Bonanno, C. W. Clark, J. D. Fassett, T. B. Lucatorto, in Proceedings of the First International Laser Science Conference, AIP Conf. Proc. No. **146**, edited by W. C. Stwalley and M. Lappo (AIP, New York, 1986), p. 409.
[10]C. H. Greene and Ch. Jungen, Adv. At. Mol. Phys. **21**, 51 (1985).
[11]C. H. Greene (private communication).
[12]M. Littman and H. Metcalf, Appl. Opt. **17**, 2224 (1978).
[13]T. W. Hänsch, Appl. Opt. **11**, 895 (1972).
[14]C. H. Greene and L. Kim, Phys. Rev. A **36**, 2706 (1987).
[15]C. -M. Lee and K. T. Lu, Phys. Rev. A **8**, 1241 (1973).
[16]R. D. Cowan, *The Theory of Atomic Structure and Spectra* (University of California Press, Berkeley, 1981).
[17]W. E. Cooke and C. L. Cromer, Phys. Rev. A **32**, 2725 (1985).
[18]S. A. Bhatti, C. L. Cromer, and W. E. Cooke, Phys. Rev. A **24**, 161 (1981). Our Eq. (10) differs from their expression by an additional factor of $\nu'^{3/2}$, since they consider the bound-bound case and we consider the bound-continuum case, which requires a different normalization (cf. Ref. 17).
[19]W. E. Cooke, S. A. Bhatti, and C. L. Cromer, Opt. Lett. **7**, 69 (1982).
[20]K. T. Lu and U. Fano, Phys. Rev. A **2**, 81 (1970).
[21]U. Fano, Phys. Rev. **124**, 1866 (1961).
[22]J. F. Kelly, J. P. Hessler, and G. Alber, Phys. Rev. A **33**, 3913 (1986).
[23]R. R. Jones and T. F. Gallagher, Phys. Rev. A **38**, 2846 (1988).
[24]V. Lange, U. Eichmann, and W. Sandner (unpublished).
[25]K. LaGattuta and Y. Hahn, Phys. Rev. Lett. **51**, 558 (1983).

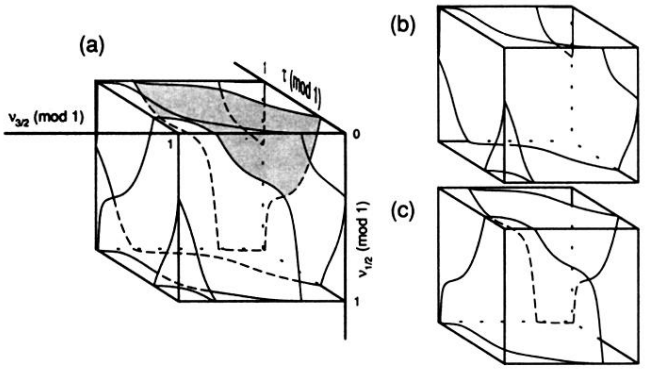

FIG. 11. (a) Three-dimensional quantum-defect surface plotted modulo 1 corresponding to the effective quantum number with respect to the Mg^+ $3P_{1/2}$ limit, the $3P_{3/2}$ limit, and the continuum phase above the $3S$ limit. For clarity, the two shaded surfaces are shown separately in (b), and the large central sheet and two small corner surfaces are shown in (c). The projection of the normal at any point on these surfaces along the three axes yields the composition of the state.